METALLURGY

Ductilization of 2.6-GPa alloys via short-range ordered interfaces and supranano precipitates

Yong-Qiang Yan[1]†, Wen-Hao Cha[2,3]†, Sida Liu[2]*, Yan Ma[4], Jun-Hua Luan[5], Ziyuan Rao[6,7], Chang Liu[1]*, Zhi-Wei Shan[1], Jian Lu[8]*, Ge Wu[1]*

Higher strength and higher ductility are desirable for structural materials. However, ultrastrong alloys inevitably show decreased strain-hardening capacity, limiting their uniform elongation. We present a supranano (<10 nanometers) and short-range ordering design for grain interiors and grain boundary regions, respectively, in fine-grained alloys based on vanadium, cobalt, and nickel, with additions of tungsten, copper, aluminum, and boron. The pronounced grain boundary–related strengthening and ductilization mechanism is realized through segregation of the short-range ordering near the grain boundary. Furthermore, the supranano ordering with a larger size has an enhanced pinning effect for dislocations and stacking faults, multiplied and accumulated in grain interiors during plastic deformation. These mechanisms promote continuously increased flow stress until fracture of the alloy at 10% strain with 2.6-gigapascal tensile stress.

Grain refinement is a practical approach to simultaneously enhance strength and ductility for coarse- and fine-grained alloys (1) that has been widely applied in industry. The yield strength of fine-grained alloys is usually <1 GPa (2, 3). Although the extreme refinement of grains to nanoscale can substantially enhance the strength, ductility decreases as a result. A gradient structure, with nano-sized grains on the surface to coarse grain in the sample interior (4), and heterostructures (with different grain sizes) (5) are successful alloy design strategies to simultaneously increase strength and ductility. The strength is enhanced because of grain boundary (GB) strengthening from the nanograin region. During plastic deformation, dislocation multiplication in the coarse grains and the generation of geometrically necessary dislocations near transition zones between the nanograin and coarse-grain regions (5) facilitate high strain-hardening rates, and thus, the ductility is enhanced. Nanostructuring for the grain interior is another important approach. Successful strategies include introductions of coherent nanoprecipitates (6–9), short-range ordering (SRO) (10–12), chemical heterogeneities (13, 14), and nanotwins (15), among others. The atomic interactions among these nanostructures and dislocations promote multiplication of dislocations in the grain interior, also enhancing strain-hardening rates. The tensile strength of these alloys can be improved to 1 to ~2 GPa. To further strengthen alloys to an ultrahigh strength level (e.g., >2.5-GPa tensile strength), various strengthening mechanisms should be introduced. However, the resultant decreased strain-hardening rate usually induces unstable necking or formation of Lüders bands, for example. The localized deformation substantially shortens uniform elongation (e.g., <5% strain for 2.5-GPa alloys) (16–18). Different from the above alloy design strategies, which focus on distribution of variant grain sizes or nanostructuring of grain interiors, here we use SRO decorating GB regions (short-range ordered interfaces) of the face-centered cubic (FCC) phase in a fine-grained FCC-BCC (body-centered cubic) dual-phase alloy, facilitated by positive interfacial interaction energy between the SRO and the FCC matrix. The short-range ordered interface can be categorized as a GB complexion (19), substantially increasing the stress barrier against dislocation motion—i.e., a higher yield strength. Therefore, more dislocations pile up near GB regions than in grain interiors during plastic deformation. The activities of dislocations (gliding and pile-up) disrupt the ordered structure of the SRO, transformed into disordered solid solution—i.e., the order-to-disorder transition. This behavior weakens stress concentrations on GB regions and thus impedes cracking from GBs of the FCC phase. Furthermore, we introduce orderings (precipitates) of <10 nm (supranano) in the grain interior of the FCC phase. The supranano (20) is a metric unit of length that is <10 nm, which is much larger than the size of SROs (<1 nm). Therefore, the supranano orderings have a stronger pinning effect for dislocations and stacking faults (SFs). Such orderings make the motion of dislocations and SFs slow, which increases the possibility of their interaction and entanglement with other moveable dislocations. This behavior promotes multiplication and accumulation of these defects upon loading. The supranano orderings are uniformly distributed in the grain interior, and thus, the distribution of the generated defects is also uniform, which alleviates stress localization. These two kinds of orderings have mutually complementary strengthening and ductilization mechanisms near GB regions and in grain interiors of the FCC phase, respectively, facilitating a high strain-hardening rate and large elongation. The received ultrahigh flow stress transforms a portion of the BCC phase (7.7% fraction) to a FCC structure during deformation.

Results and discussion
Microstructure and composition

To realize ultrahigh yield strength, we refined the grain size and introduced a secondary harder phase by thermal treatments and rolling processes. The reduced grain size shortens the mean-free path of dislocations in the grain interior and enhances interactions of the dislocations with the short-range ordered GB regions in the FCC phase. We then performed thermal aging to trigger formation of the precipitate ordering, facilitating large uniform elongation. The received VCoNi-W-Cu-Al-B alloy has a dual phase structure (Fig. 1, A and B), composed of FCC and $L2_1$ (an ordered BCC phase) structures, with an average grain size of 1 μm for both phases (fig. S1). The FCC phase has an area fraction of 78.7%, dominating the main structure of the material. Further reduction in the fraction of the FCC phase might induce embrittlement of the alloy (21). The structure evolution of the alloy during thermal and mechanical treatments is shown in fig. S2. The compositions of the FCC and $L2_1$ phases are $Ni_{37}Co_{34}V_{27}Al_2$ atomic % (at %) and $Co_{31}V_{25}Ni_{25}Al_{18}Cu_{0.5}W_{0.5}$ at % (Fig. 1, C and D), respectively. Some tiny boride nanoparticles with an average diameter of 240 nm discontinuously embed between adjacent FCC-BCC phase boundaries (fig. S3). The $L2_1$ phase and boride nanoparticles may also contribute to the strengthening effect. The $L2_1$ phase reveals a typical superlattice feature in a selected-area electron diffraction (SAED) pattern (Fig. 1B$_1$). The SAED pattern of the FCC phase depicts very weak diffraction spots of $L1_2$ structure among the matrix lattice (Fig. 1B$_2$), which is different from that of other $L1_2$ nanoprecipitated alloys (6–9). We performed atom-resolved investigations from the <1 1 2> zone axis (Fig. 1F) using aberration-corrected scanning transmission electron microscopy (STEM). The

[1]Center for Advancing Materials Performance from the Nanoscale (CAMP-Nano), Hysitron Applied Research Center in China (HARCC) and Center for Alloy Innovation and Design (CAID), State Key Laboratory for Mechanical Behavior of Materials, Xi'an Jiaotong University, Xi'an, China.

[2]Laboratory for Multiscale Mechanics and Medical Science, SV LAB, School of Aerospace, Xi'an Jiaotong University, Xi'an, China. [3]Faculty of Georesources and Materials Engineering, RWTH Aachen University, Aachen, Germany.

[4]Department of Materials Science and Engineering, Delft University of Technology, Delft, Netherlands.

[5]Inter-University 3D Atom Probe Tomography Unit, Department of Mechanical Engineering, City University of Hong Kong, Hong Kong, China. [6]Max Planck Institute for Sustainable Materials, Düsseldorf, Germany. [7]National Engineering Research Center of Light Alloy Net Forming, Shanghai Jiao Tong University, Shanghai, China. [8]Centre for Advanced Structural Materials, Department of Materials Science and Engineering, City University of Hong Kong, Hong Kong, China.

*Corresponding author. Email: gewuxjtu@xjtu.edu.cn (G.W.); chang.liu@xjtu.edu.cn (C.L.); sidaliu@xjtu.edu.cn (S.L.); jianlu@cityu.edu.hk (J.L.)

†These authors contributed equally to this work.

Fig. 1. Structure of the SS-alloy (containing both SRO and S-L1$_2$ particle in the FCC phase).
(**A**) Reconstructed three-dimensional EBSD inverse pole figure probed from normal direction (y), rolling direction (z), and transverse direction (x). (**B**) Phase image of the square region in (A), showing the FCC-BCC dual-phase structure. Area fractions of FCC and BCC phases are 78.7 and 21.3%, respectively. (**B$_1$** and **B$_2$**) SAED patterns of the two phases, probed from BCC <0 1 1> and FCC <0 1 1> zone axes, respectively. (**C**) One-nanometer-thick side slice of the three-dimensional reconstruction of a typical atom probe tomography (APT) dataset, showing Al-enriched and Al-depleted regions highlighted by an isoconcentration surface in terms of an Al threshold value of 12 at %. The APT tip may be sampled from the area similar to the cyan dashed square region in (B), with FCC phase embedded in BCC phase. (**D**) One-dimensional compositional profile across the region indicated with the arrow in (C), showing the compositions of the FCC and BCC (L2$_1$) phases. The light shadows indicate statistical errors in terms of the standard deviations. (**E**) Schematic illustration from MD calculation, depicting the segregation and precipitation behaviors of SRO and L1$_2$ particle near GB region and in grain interior, respectively. (**F**) Aberration-corrected high-angle annular dark-field (HAADF) STEM image of the FCC phase, probed from <1 1 2> zone axis. (**G**) Fast Fourier transformation (FFT) image of (F), showing the main diffraction spots of the FCC matrix (cyan dashed circles), weak diffraction spots of the S-L1$_2$ particles (yellow dashed circles), and blurry diffraction disks of the SRO (pink arrows and dashed circles). (**H**) Enlarged HAADF-STEM image (upper panel) of the dashed green rectangle region in (F), showing the atoms of an ordered particle and the disordered matrix arranged with and without periodic Z-intensity, respectively (lower panel). a.u., arbitrary units. (**I** and **J**) IFT images of (F) generated by using the masks of SRO and S-L1$_2$ diffraction spots and disks in (G), respectively, highlighting the SRO and S-L1$_2$ regions in real space. (**K**) Combined IFT image, generated by using the masks of FCC, SRO, and S-L1$_2$ diffraction (d) spots and disks in (G), respectively, showing the configurations of the SRO and S-L1$_2$ particle in the FCC matrix. The insets are enlarged images of the solid square regions and reveal lattice structures of the SRO and S-L1$_2$ particle, coherent with the FCC matrix.
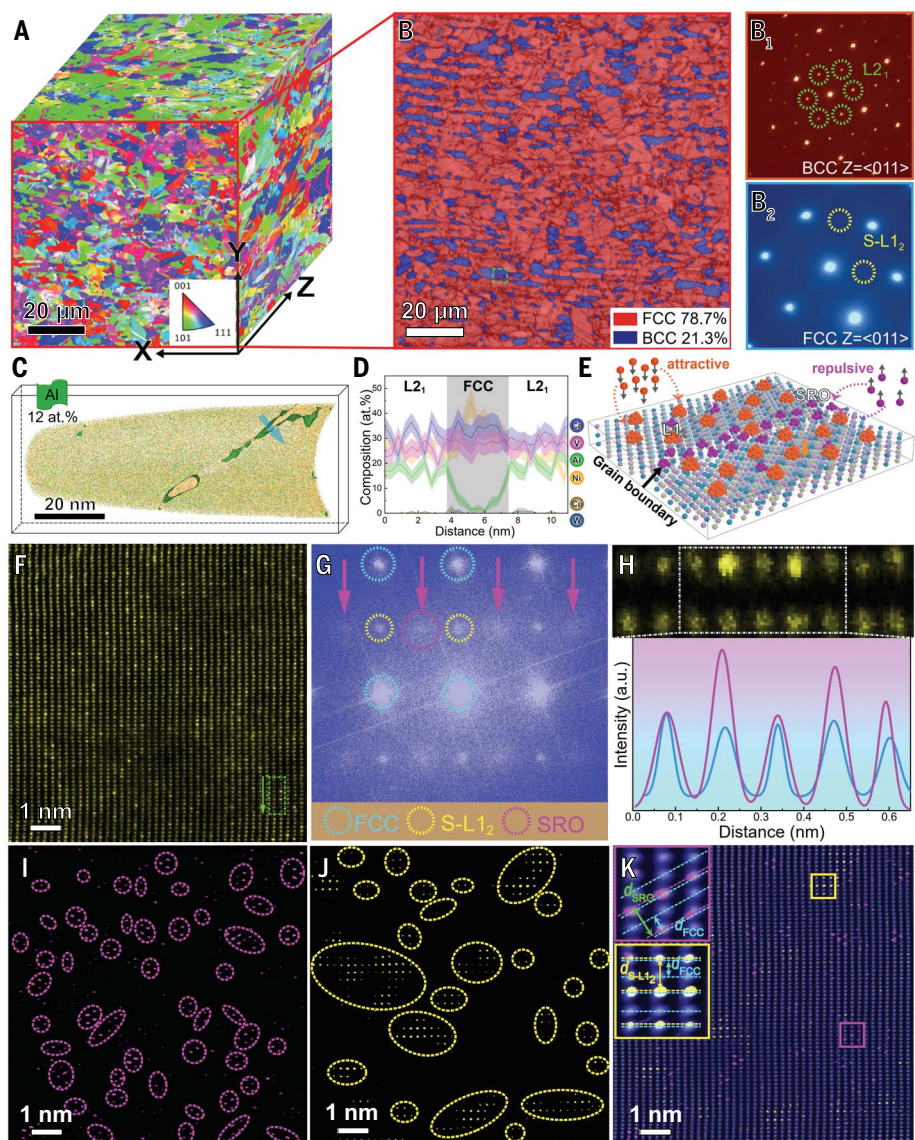
result shows a major disordered solid solution structure but with occasionally brighter atoms (Fig. 1, F and H) within the matrix lattice. A careful inverse Fourier transformation (IFT) analysis (Fig. 1, I and J) shows that the brighter atoms are not randomly distributed. Rather, they aggregate into two kinds of local orderings, SRO and supranano L1$_2$ (S-L1$_2$) particle. Because of their different crystalline structures, the S-L1$_2$ particles are mainly formed by nucleation in the FCC matrix instead of growth from the SRO during aging. In this study, the fractions of the S-L1$_2$ particle and SRO are 30 and 22%, respectively, in the FCC phase (fig. S4). The size of S-L1$_2$ particles and SRO are 0.5 to ~4 nm and <1 nm, respectively (Fig. 1, I and J). Therefore, the corresponding diffraction

spots of the S-L1$_2$ particles are substantially weaker than those of previously reported L1$_2$ nanoprecipitated alloys (6–9), which usually have a much larger precipitation size of 10 to tens of nanometers. Furthermore, the diffraction feature of the S-L1$_2$ particles reveals weak spots (Fig. 1G, dashed yellow circles) compared with blurry disks for SRO (Fig. 1G, dashed pink circles) because of a much larger size of the S-L1$_2$ particles. The SROs with heterogeneous structures and compositions are generally believed to multiply dislocations during plastic deformation, improving ductility of the materials (10–12). In fine-grained alloys, the volume fraction of GB is large, so that the GB structure has a big influence on mechanical behavior. We performed careful composition investi-

gation on GB regions of the FCC phase using electron probe microanalysis (EPMA), showing the absence of B (fig. S3). Therefore, the change of atomic packing structure near GB regions by segregation of B (22, 23) can be ruled out. We then performed molecular dynamics (MD) simulation to study GB segregation tendency of the SRO and S-L1$_2$ particles in the FCC phase. The result shows that the interfacial interaction energy between the SRO and the FCC matrix lattice is positive, which indicates a repulsive interaction (Fig. 1E and fig. S5). This behavior facilitates segregation of the SRO toward GB regions of the FCC phase. By contrast, the interfacial interaction energy is negative for the case of S-L1$_2$ particles, promoting their precipitation in grain interiors (Fig. 1E and fig. S5).
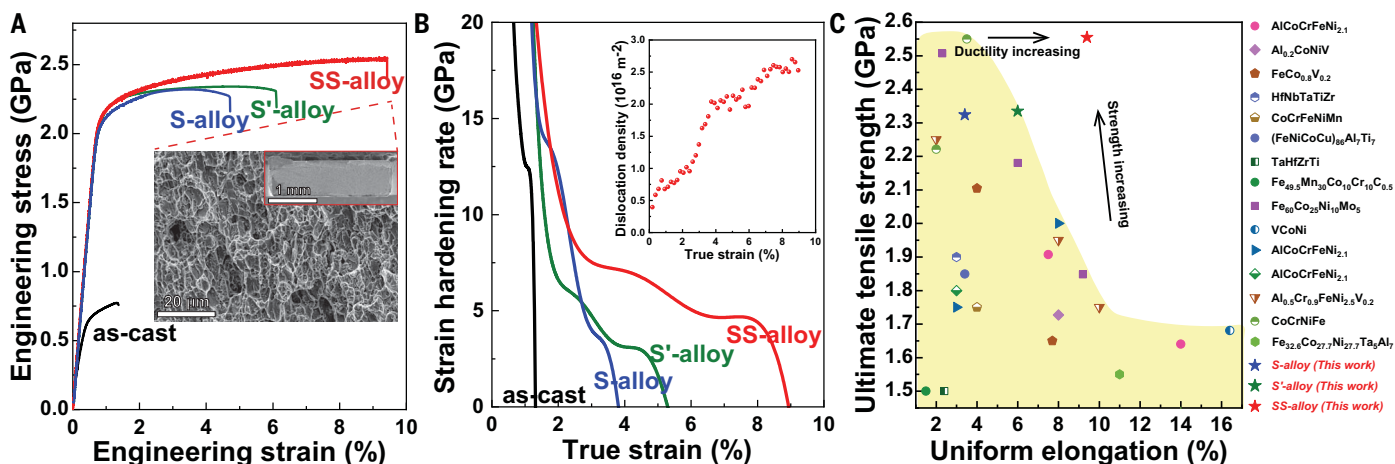
Fig. 2. Room-temperature tensile property of the SS-alloy. (**A**) Engineering tensile stress-strain curves of the SS-alloy, S'-alloy, S-alloy, and as-cast alloy. The insets are fracture surface of the SS-alloy sample after tensile testing, revealing dimple-type pattern. (**B**) Strain-hardening rate evolutions of the alloys during tensile straining. (Inset) Dislocation density evolution of the FCC phase in the SS-alloy during tensile straining. (**C**) UTS versus uniform elongation relation of the alloys in the current study, compared with that of other ultrastrong CCAs (8, 16, 18, 39–50).

The experimental observations (Fig. 3G₁ and fig. S6) confirm this theoretical result.

Mechanical properties

We performed identical tensile tests on as-cast alloy, S-alloy (containing SRO in the FCC phase), S'-alloy, and SS-alloy (containing both SRO and S-L1₂ particle in the FCC phase) (Fig. 2A). The as-cast alloy has a yield strength of 0.7 GPa and total elongation of 1.3% strain. The yield strength and total elongation increase to 2.1 GPa and 4.7% strain, respectively, after additional rolling and thermal treatments for the S-alloy. The enhancement of mechanical property is mainly due to the refined dual-phase structure and embedded SRO in the FCC phase (fig. S7). The ultimate tensile strength (UTS) is 2.3 GPa at 2.6% strain, and strain softening occurs subsequently. After an additional 5 hours of aging at 500°C, the yield strength and total elongation increase to 2.2 GPa and 6.0% strain, respectively, for the S'-alloy. The UTS is still 2.3 GPa but with a much larger uniform elongation of 4.9% strain. With further aging time (20 hours' aging at 500°C), the received SS-alloy has a further increased uniform elongation of 9.5% strain and a yield strength of 2.2 GPa. We also conducted identical tensile tests on a much thicker SS-alloy, and its mechanical properties do not substantially change (fig. S8). The morphology of the fracture surface reveals a dimple-type pattern (Fig. 2A, inset), a ductile signature of the alloy. After yielding, strain hardening lasts until fracture of the alloy, inducing an ultrahigh UTS of 2.6 GPa (Fig. 2, A and B). The structure difference of the SS-alloy is the addition of S-L1₂ particles after thermal aging compared with the reference S-alloy, facilitating an increased yield strength and much higher strain-hardening rate (Fig. 2B). We calculated dislocation density of the FCC

phase in the SS-alloy on the basis of in situ synchrotron x-ray diffraction during tensile tests. The result shows that dislocation density increases during deformation. The dislocation density of the FCC phase continuously increases to $>1 \times 10^{16}$ m^{-2} after 2.6% strain (Fig. 2B, inset), where that is the reference S-alloy's UTS point. Such a high density of dislocations is comparable to that of severely plastic deformed alloys (24), promoting a high strain-hardening rate and preventing strain softening as in the reference S-alloy. Dislocation motion can also be activated in the ordered BCC phase during plastic deformation, although this phase is generally known to be brittle (25, 26). We show that the ultrahigh flow stress induces BCC-to-FCC phase transformation, and the confinement deformation activates dislocation motions in the BCC phase. We compared the mechanical properties of the SS-alloy with those of other ultrahigh-strength (UTS > 1.5 GPa) compositional complex alloys (CCAs) at room temperature (Fig. 2C and fig. S9). For a fair comparison, we do not include the data of dilute alloys or the alloys revealing nonuniform deformations (e.g., with post-yielding, largely serrated plastic flow). To highlight strain-hardening capacity at ultrahigh flow stress, UTS versus uniform elongation (Fig. 2C) and yield strength versus hardened strength relations (fig. S9) are plotted. The SS-alloy shows a good combination of UTS, uniform elongation, and strain-hardening capacity. The existing alloys with UTS exceeding 2.5 GPa usually have very limited uniform elongation (<5% strain). Furthermore, previous ultrastrong alloys show limited strain-hardening capacity if their yield strength is >2.0 GPa, restricting further hardening to UTS of 2.6 GPa. The mechanical instability of these ultrastrong alloys is usually attributed to early

necking by strain localization (1). Compared with the reference S-alloy, the additional supranano ordering in the SS-alloy can solve this problem.

Deformation mechanisms

The atomic interactions from the supranano particles in the FCC phase facilitate the "extra" strain hardening compared with that of the reference S-alloy. Furthermore, we performed TEM and aberration-corrected STEM investigations on the deformed FCC phase to reveal deformation mechanisms (Fig. 3). The initial FCC phase already contains a large number of dislocations (Fig. 3A), consistent with the synchrotron x-ray diffraction result (dislocation density of 4.0×10^{15} m^{-2}; Fig. 2B, inset). A high density of dislocations is introduced by a cold-rolling process, inducing the high yield strength of the SS-alloy. We performed careful TEM investigations (fig. S10) on hot-rolled recrystallized alloys with or without thermal aging [the alloys have a much larger grain size of 2 μm (fig. S2) and reduced density of dislocations], respectively, showing that the formation of SRO and S-L1₂ particles is similar to that of the S-alloy and SS-alloy. This indicates that grain size and dislocation density do not have substantial influence on the formation of SRO and S-L1₂ particles in the FCC phase. The dislocation density should have dynamic increasing during plastic deformation to maintain strain-hardening capacity (24, 27–29); otherwise, subsequent necking-induced instability prevails, which decreases the ductility of the alloy (S-alloy; Fig. 2A). In the current SS-alloy, dislocation density has substantial improvements during the whole deformation process, shown by both TEM (Fig. 3, A to D) and synchrotron x-ray diffraction (Fig. 2B, inset) results. The plasticity carriers are mainly dislocations at the beginning of plastic deformation
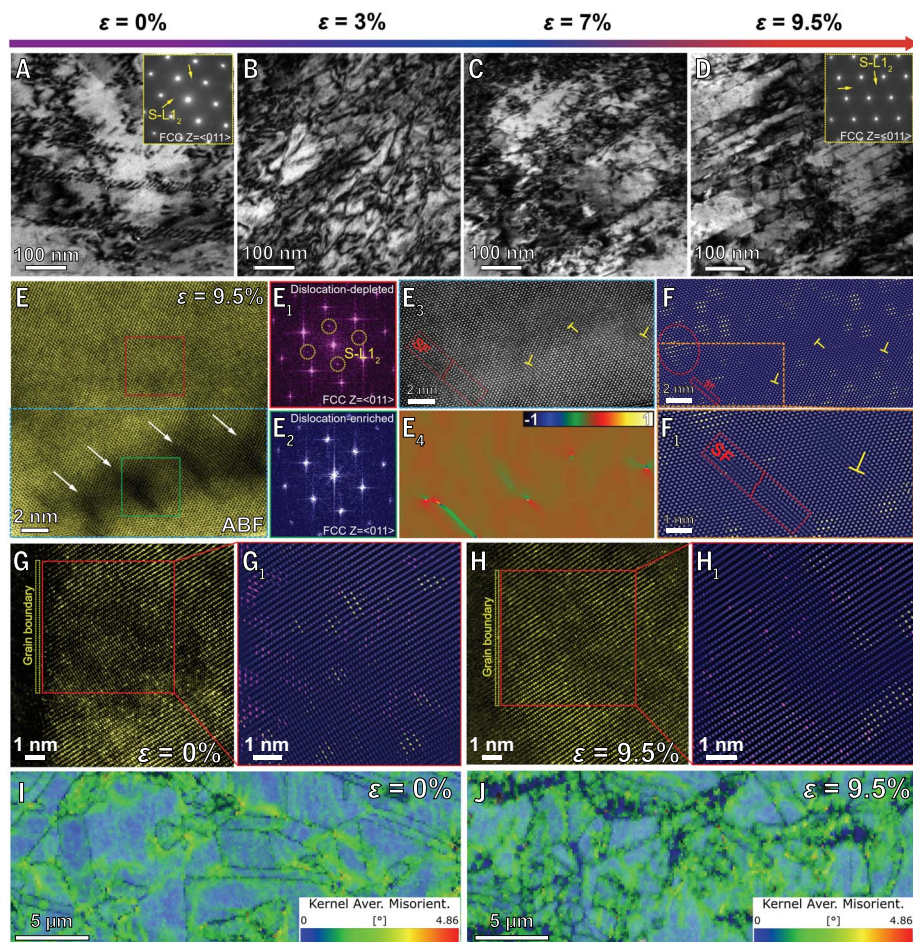
Fig. 3. Structure evolution of the FCC phase in the SS-alloy upon tension. (**A** to **D**) Bright-field TEM images of the FCC phase under different tensile strains, showing evolutions of dislocations and SFs. The TEM images are in two-beam condition probed from <0 1 1> direction with a g = {1 1 −1} vector. The insets in (A) and (D) are corresponding SAED patterns probed from <0 1 1> zone axis, showing weakening of S-L1$_2$ diffraction spots after tension. (**E**) Aberration-corrected annular bright-field (ABF) STEM image of the FCC phase after 9.5% tensile straining. The upper and lower regions contain few and substantial (denoted by white arrows) dislocations, respectively. (**E$_1$** and **E$_2$**) FFT patterns derived from the red and green square regions in (E), respectively, showing disappearing of S-L1$_2$ diffraction spots in dislocation-enriched regions. (**E$_3$**) Enlarged aberration-corrected HAADF-STEM image of the dislocation-enriched region in (E), showing a SF on the left and three dislocations on the right. (**E$_4$**) Corresponding strain mapping of (E$_3$) based on geometrical phase analysis, revealing strain localizations by SF and dislocations. (**F**) Combined IFT image generated from (E$_3$), showing interactions among dislocations or SFs and S-L1$_2$ particles. (**F$_1$**) Enlarged image of the dashed rectangle region in (F). (**G**) Aberration-corrected HAADF-STEM image of a FCC region near GB before tension, probed from <1 1 2> zone axis. (**G$_1$**) Enlarged combined IFT image generated from the red square region in (G), showing enrichment of SROs near GB. (**H**) Aberration-corrected HAADF-STEM image of a FCC region near GB after 9.5% tensile straining, probed from <1 1 2> zone axis. (**H$_1$**) Enlarged combined IFT image generated from the red square region in (H). The distribution of SROs is uniform across GB, indicating disruption of the ordering by motion of dislocations. (**I**) Kernel average misorientation (KAM) mapping of the SS-alloy before tension. Strains are concentrated in most GB regions, which may be due to the enrichment of SROs near GB. (**J**) KAM mapping of the SS-alloy after 9.5% tensile straining. Strain concentrations are uniformly distributed across GB and grain interior.

ticles may lower the degree of precipitation strengthening in the FCC phase, the dislocations can be effectively multiplied to counteract this softening and further provide strain hardening. This effect is mainly due to the hindering of dislocation motion by the S-L1$_2$ particles ahead. Moreover, there are almost no S-L1$_2$ particles on SFs, indicating another order-to-disorder transition effect by SF motion (Fig. 3F$_1$). Larger-sized S-L1$_2$ particles still exist on two ends of the SF (Fig. 3F$_1$), which impedes the SF's propagation. One particle (~3-nm size) is highlighted by a red dashed circle in Fig. 3F, which shows how it is much larger than the average particle size (1.4 nm; fig. S4). Therefore, more SFs are generated from other planes, refining the microstructure (Fig. 3D). The dynamically shortened mean-free path of dislocations elevates the stress barrier against dislocation motion, further enhancing the strain-hardening capacity. The SROs are much smaller than S-L1$_2$ particles, and thus, the pinning effect for dislocations and SFs is less pronounced. This explains the shorter uniform elongation of the reference S-alloy compared with that of the SS-alloy (Fig. 2A). One may argue that it is better to replace SROs with S-L1$_2$ particles to enhance the ductility. That argument will be correct if the SROs only precipitated in the grain interior.

The current SRO provides an "extra" ductilization mechanism, which cannot be realized by the S-L1$_2$ particles. The S-L1$_2$ particles precipitate in grain interiors, but the SRO has the opposite tendency, segregating near GB regions of the FCC phase (Fig. 3, G and G$_1$). This segregation scenario induces strain concentrations on GBs (Fig. 3I). This effect elevates the stress barrier against nucleation of dislocations from GBs, enhancing the yield strength. However, it is reported that a large number of dislocations may pile up on the strain-concentrated GBs during plastic deformation (4, 30, 31), favoring generation of microcracks. This effect is severe in conventional ultrafine-grained alloys, owing to the short mean-free path of dislocations. In the current SS-alloy after tensile deformation, however, the SROs are uniformly distributed across the GB region and grain interior of the FCC phase (Fig. 3H$_1$)—the SRO near the GB region is substantially weakened. This indicates a higher probability of order-to-disorder transition events of SRO near the GB region compared with the grain interior because of the more intense dislocation activities. The complex SF energy and antiphase boundary energy of the CCAs decay after dislocation glide (32), and the dislocation activities inevitably distort the local atomic packing structure of the SRO (33), promoting the transition toward random solid solution. Because SROs have a weaker pinning effect for dislocations than S-L1$_2$ particles have, the dislocation pile-up
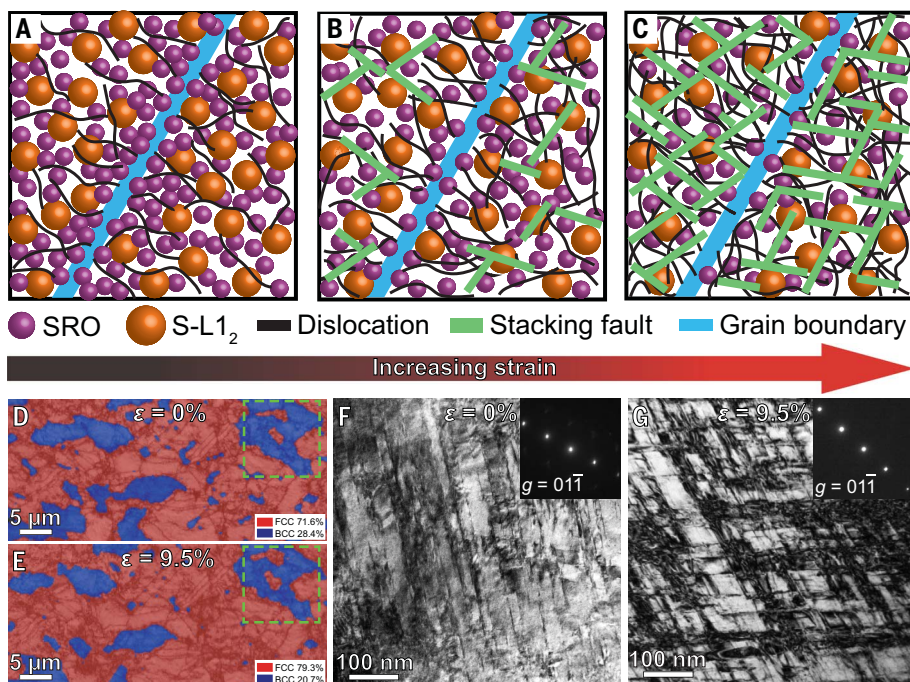
(3% strain; Fig. 3B), and then SFs initiate subsequently (Fig. 3, C and D). The diffraction spots of the S-L1$_2$ phase become less pronounced after deformation (Fig. 3, A and D, insets), indicating an order-to-disorder transition. This behavior is further demonstrated by an in situ TEM tension experiment (fig. S11). Aberration-corrected high-resolution STEM observations reveal that dislocation-enriched regions contain much fewer S-L1$_2$ particles (Fig. 3, E$_3$ and F). This indicates that the motion of dislocations disrupts the ordered particles, transformed into disordered solid solution. Although the order-to-disorder transition of the S-L1$_2$ par-

Fig. 4. Deformation mechanism of the SS-alloy. (**A** to **C**) Schematic illustration showing the structure evolution of the FCC phase upon tension. SRO and S-L1$_2$ particles are enriched near GB and in grain interior, respectively, before tension (A). During tension, dislocation activities near GB induce order-to-disorder transition of the SROs near GB, releasing strain concentrations (B). Large numbers of dislocations and SFs are multiplied and accumulated in grain interiors because of the enhanced pinning effect from S-L1$_2$ particles compared with that from SROs (C). (**D** and **E**) EBSD phase mapping images of the same region in the SS-alloy before and after tension, showing BCC-to-FCC phase transformation from the phase boundary. (**F** and **G**) TEM images of the ordered BCC phase before and after tension, probed from <0 1 1> direction with a g = {0 1 –1} vector. The insets are corresponding SAED patterns.

configuration is also weaker. The disordering of the SROs with a weaker dislocation pile-up feature substantially relieves strain concentrations on the GB regions, impeding microcrack generation. Meanwhile, the uniformly distributed SRO and S-L1$_2$ particles in the grain interior favor the uniform accumulation feature of dislocations. As a result, strain concentration scenarios are similar in the GB region and grain interior of the FCC phase (Fig. 3J). This strain delocalization mechanism postpones crack generation and prolongs the elongation. The uniformly multiplied dislocations in the grain interiors and GB regions of the FCC phase promote strain hardening.

The ordered BCC phase is usually harder than the FCC phase, contributing to a higher yield strength but reduced ductility (*21*). We performed electron backscattered diffraction (EBSD) investigations on the same region of an SS-alloy sample before and after tension (Fig. 4, D and E), which showed that the fraction of the FCC phase increases from 71.6 to 79.3% upon deformation, indicating a strain-induced BCC to FCC phase transformation phenomenon. This corresponds well with the in situ synchrotron x-ray diffraction results during tensile test (fig. S12). The BCC-to-FCC phase

transformation usually occurs at the crack tip, where it is under an ultrahigh stress level (*34, 35*). It is suggested that shearing of the lattice on a {0 1 1}$_{BCC}$ habit plane in the <1 –1 1>$_{BCC}$ direction induces this phase transformation, known as the Nishiyama-Wassermann model (*36*). In the current SS-alloy, ~2.6-GPa flow stress is an ultrahigh level among the reported CCAs (Fig. 2C). The boundary of a FCC region migrates into the adjacent BCC region (Fig. 4, D and E, green dashed square), but the SS-alloy seldom reveals nucleation of the FCC phase inside a BCC grain upon deformation. This indicates that the BCC-to-FCC phase transformation mainly occurs from the FCC-BCC phase boundary. The FCC phase, BCC phase, and boride nanoparticles at the FCC-BCC phase boundary have different intrinsic mechanical properties (namely, differences in shear modulus and Burgers vector), and thus, stress localization preferably occurs at the phase boundary. Therefore, the stress level should be much higher than the average flow stress of the alloy, promoting the BCC-to-FCC phase transformation. The displacive movements of lattice planes can relieve stress concentrations. For comparison, we also performed identical mechanical tests on reference alloys without W

and Cu and without B, W, and Cu (fig. S13). The reference alloys have reduced yield strength and elongation, which in turn demonstrates the strengthening and ductilization effect from the boride nanoparticles in the SS-alloy. Dislocation motion can be activated in the BCC phase (Fig. 4, F and G) and boride nanoparticles (fig. S3, C and D), although the L2$_1$ BCC phase (*25, 26*) and the boride are generally known to be brittle. Because the FCC phase has the highest fraction, has a larger grain size, and causes the ductile deformation mechanism in the SS-alloy, the dislocation motions in the brittle phases are mainly due to confinement deformation with the FCC phase (*37, 38*). Geometrically necessary dislocations generated in the softer FCC phase pile up near the phase boundaries, rendering back stress in the softer FCC phase and forward stress in the harder phases (the hetero-deformation–induced stresses) (*5*). This hetero-deformation mode near the phase boundaries can also induce strain hardening of the different phases (*5*). The harder phases should have globular-like morphology and be distributed uniformly among the alloy, delocalizing stress concentrations on the phase boundaries. These behaviors further ductilize the SS-alloy. If the plastic flow stress of an alloy could not be maintained at such a high level (e.g., traditional dual-phase alloys with low flow stress), the BCC-to-FCC transformation will not occur. Therefore, the strengthening and ductilization mechanisms from the SRO and S-L1$_2$ particles (Fig. 4, A to C) in the FCC phase are the key preconditions for this behavior.

Conclusions

In summary, we present a ductilization strategy for 2.6-GPa alloys through short-range ordered interfaces and supranano precipitates. The supranano precipitates are L1$_2$ particles with a diameter of 0.5 to ~4 nm, coherent with the FCC solid-solution matrix. They have a stronger pinning effect for dislocations and SFs during plastic deformation compared with SROs, triggering multiplication and accumulation of dislocations in grain interiors of the FCC phase and thus a higher strain-hardening rate. The SROs have positive interfacial interaction energy with the FCC matrix, promoting their segregation near GB regions of the FCC phase. This configuration is helpful for the enhancement of yield strength. The less pronounced pinning effect for dislocations favors dislocation motion near GB regions of the FCC phase, inducing the order-to-disorder transition of the SROs. This behavior, together with the weaker dislocation–pile-up configuration, relieves strain concentrations at GBs of the FCC phase during plastic deformation. Consequently, strain variation is uniformly distributed across GB regions and grain interiors of the FCC phase. Furthermore, the BCC-to-FCC phase transformation occurs at FCC-BCC

phase boundaries because of an ultrahigh stress level during plastic deformation. The hetero-deformation mode near the phase boundaries can also induce strain hardening, and the displacive phase transformation relieves stress concentrations at the phase boundaries, further ductilizing the alloy. The combined precipitation structuring by supranano ordering and interfacial decoration by SRO offer a strategy to ductilize ultrastrong alloys, achieving large uniform elongation with continuous strain hardening until fracture, especially for alloys exceeding 2.5-GPa tensile strength.

REFERENCES AND NOTES

1. F. C. Campbell, Ed., *Elements of Metallurgy and Engineering Alloys* (ASM International, 2008).
2. K. Rahman, V. Vorontsov, D. Dye, *Acta Mater.* **89**, 247–257 (2015).
3. F. Khodabakhshi, M. Haghshenas, H. Eskandari, B. Koohbor, *Mater. Sci. Eng. A* **636**, 331–339 (2015).
4. K. Lu, *Science* **345**, 1455–1456 (2014).
5. Y. Zhu, X. Wu, *Prog. Mater. Sci.* **131**, 101019 (2023).
6. T. Yang *et al.*, *Science* **362**, 933–937 (2018).
7. J. He *et al.*, *Acta Mater.* **102**, 187–196 (2016).
8. L. Han *et al.*, *Nature* **608**, 310–316 (2022).
9. Y. Yang *et al.*, *Nature* **595**, 245–249 (2021).
10. E. Ma, C. Liu, *Prog. Mater. Sci.* **143**, 101252 (2024).
11. X. Chen *et al.*, *Nature* **592**, 712–716 (2021).
12. L. Wang *et al.*, *Nat. Mater.* **22**, 950–957 (2023).
13. Z. Lei *et al.*, *Nature* **563**, 546–550 (2018).
14. Q. Ding *et al.*, *Nature* **574**, 223–227 (2019).
15. K. Lu, L. Lu, S. Suresh, *Science* **324**, 349–352 (2009).
16. H. Kwon *et al.*, *Acta Mater.* **248**, 118810 (2023).
17. M. Niu *et al.*, *Acta Mater.* **179**, 296–307 (2019).
18. J. Man *et al.*, *J. Mater. Sci. Technol.* **177**, 79–84 (2024).
19. P. R. Cantwell *et al.*, *Acta Mater.* **62**, 1–48 (2014).
20. G. Wu, K.-C. Chan, L. Zhu, L. Sun, J. Lu, *Nature* **545**, 80–83 (2017).
21. J. He *et al.*, *Acta Mater.* **62**, 105–113 (2014).
22. T. Yang *et al.*, *Science* **369**, 427–432 (2020).
23. R. Wu, A. J. Freeman, G. B. Olson, *Science* **265**, 376–380 (1994).
24. B. B. He *et al.*, *Science* **357**, 1029–1032 (2017).
25. Y. Mu *et al.*, *Acta Mater.* **232**, 117975 (2022).
26. X. Chen *et al.*, *J. Mater. Res. Technol.* **25**, 3273–3284 (2023).
27. Y. Li *et al.*, *Science* **379**, 168–173 (2023).
28. H. Li *et al.*, *Nature* **604**, 273–279 (2022).
29. B. Xu *et al.*, *Nat. Mater.* **23**, 755–761 (2024).
30. Y. Wang, M. Chen, F. Zhou, E. Ma, *Nature* **419**, 912–915 (2002).
31. R. O. Ritchie, *Nat. Mater.* **10**, 817–822 (2011).
32. Q.-J. Li, H. Sheng, E. Ma, *Nat. Commun.* **10**, 3563 (2019).
33. Y. Yang *et al.*, *Nat. Commun.* **15**, 1402 (2024).
34. S. J. Wang *et al.*, *Nat. Commun.* **5**, 3433 (2014).
35. J. Zhang *et al.*, *Nat. Commun.* **12**, 2218 (2021).
36. Z. Nishiyama, *Sci. Rep. Tohoku Univ.* **23**, 637 (1934).
37. P. Shi *et al.*, *Science* **373**, 912–918 (2021).
38. Q. Wu *et al.*, *Nat. Commun.* **13**, 4697 (2022).
39. J. Ren *et al.*, *Nature* **608**, 62–68 (2022).
40. T. J. Jang *et al.*, *Nat. Commun.* **12**, 4703 (2021).
41. H. Chung *et al.*, *Nat. Commun.* **14**, 145 (2023).
42. B. Schuh *et al.*, *Acta Mater.* **142**, 201–212 (2018).
43. H. Shahmir, J. He, Z. Lu, M. Kawasaki, T. G. Langdon, *Mater. Sci. Eng. A* **676**, 294–303 (2016).
44. R. Zheng, J. Chen, W. Xiao, C. Ma, *Intermetallics* **74**, 38–45 (2016).
45. H. Huang *et al.*, *Adv. Mater.* **29**, 1701678 (2017).
46. J. Su, D. Raabe, Z. Li, *Acta Mater.* **163**, 40–54 (2019).
47. J. M. Park *et al.*, *Mater. Res. Lett.* **9**, 315–321 (2021).
48. S. R. Reddy *et al.*, *Sci. Rep.* **9**, 11505 (2019).
49. I. Wani *et al.*, *Mater. Sci. Eng. A* **675**, 99–109 (2016).
50. L. Wang *et al.*, *Acta Mater.* **216**, 117121 (2021).

SUPPLEMENTARY MATERIALS

science.org/doi/10.1126/science.adr4917
Materials and Methods
Figs. S1 to S13
References (*51–68*)

Submitted 3 July 2024; accepted 20 December 2024
10.1126/science.adr4917